Eur. Phys. J. B **19**, 475–490 (2001)

THE EUROPEAN
PHYSICAL JOURNAL B
EDP Sciences

Antiferromagnetic order and phase transitions in GdS as studied with X-ray resonance-exchange scattering

Th. Brückel[1,a], D. Hupfeld[1], J. Strempfer[2], W. Caliebe[1], K. Mattenberger[3], A. Stunault[4], N. Bernhoeft[5], and G.J. McIntyre[6]

[1] Forschungszentrum Jülich, Institut für Festkörperforschung, 52425 Jülich, Germany
[2] Advanced Photon Source at Argonne National Laboratory, LOM 433 - D 008, 9700 South Cass Avenue, Argonne, IL 60439, USA
[3] Eidgenössische Technische Hochschule Zürich Hönggerberg (ETH), Labor für Festkörperphysik, 8093, Zürich, Switzerland
[4] European Synchrotron Radiation Facility (ESRF), BP 2 20, 38043 Grenoble Cedex 9, France
[5] CEA Grenoble, DRFMC, 38054 Grenoble, France
[6] Institut Laue-Langevin, BP 156, 38042 Grenoble Cedex 9, France

Received 19 November 1999 and Received in final form 12 December 2000

Abstract. We report on X-ray resonance exchange and neutron scattering of metallic GdS. At the $\mathrm{L_{II}}$ and $\mathrm{L_{III}}$ absorption edges of Gd, resonance enhancements of more than two orders of magnitude over the non-resonant magnetic scattering are observed. Polarisation analysis proves that these enhancements are due to dipolar transitions from the $2p$ to the $5d$ states. The branching ratio between the $\mathrm{L_{II}}$ and $\mathrm{L_{III}}$ edges of 2.5 suggests a polarisation of the $5d$ electrons in the ground state. The antiferromagnetic order is of type II in the fcc lattice. Single crystal diffraction of hot neutrons suggests that the spin direction lies within the (111) planes with a value for the sublattice magnetisation of 6.51(3) μ_B. The critical exponent for the sublattice magnetisation has a value of $\beta = 0.38(2)$ in agreement with a pure Heisenberg model. Above T_N, a sharp component persists in the critical diffuse scattering. Lattice distortions give indications for two additional low-temperature phase transitions at about 49 K and 32 K. We argue that these transitions are not connected to spin reorientations and discuss the possible influence of fourth-order exchange interactions.

PACS. 75.25.+z Spin arrangements in magnetically ordered materials (including neutron and spin-polarized electron studies, synchrotron-source X-ray scattering, etc.) – 75.40.Cx Static properties (order parameter, static susceptibility, heat capacities, critical exponents, etc.) – 78.70.Ck X-ray scattering

1 Introduction

Starting in the 60s, the magnetic properties of the rare-earth monochalcogenides have been widely investigated. A review is given in [1]. At room temperature, these compounds have the fcc NaCl type structure. GdS is one representative of this type of compounds. In a simple picture, Gd is trivalent ($\mathrm{Gd^{3+}}$ $\mathrm{S^{2-}}$) with one delocalised electron per Gd atom in the conduction band giving rise to metallic conductivity. The $\mathrm{Gd^{3+}}$ ion possesses a half-filled $4f$-shell with seven unpaired spins, leading to a $^8\mathrm{S}_{7/2}$ ground state. Due to this isotropic ground state, GdS is thought to be a model example of a Heisenberg system. The electronic structure of GdS has been studied with photoemission experiments [2]; a review is given in [3]. The $4f^7$ states have a width of about 1.2 eV with a center of gravity at 8.9 eV below the Fermi energy E_F. The $3p^6$ valence band extends from 7 eV to 2.7 eV below E_F. The metallic behaviour of GdS is due to one free electron per Gd atom of mostly d character. The conduction band starts at about 1.5 eV below E_F and exhibits crystal-field split $5d$ states with a separation between t_{2g} and e_g of 1.6 eV. In the paramagnetic state, the magnetic moment per Gd atom is 8.2 (1) μ_B, which is larger than the free ion value of 7.94 μ_B. This difference has been attributed to a contribution of the conduction electrons [3]. In the framework of molecular field theory, exchange constants for nearest and next-nearest neighbours $J_1 \approx -0.4$ K and $J_2 \approx -0.9$ K can be estimated from the values of the paramagnetic Curie temperature (≈ -110 K) and the Néel temperature (≈ 60 K) of GdS [4]. Both, the nearest- and next-nearest-neighbour exchange are antiferromagnetic. Besides the antiferromagnetic superexchange

---

[a] e-mail: `T.Brueckel@fz-juelich.de`

interaction, an antiferromagnetic exchange interaction of RKKY type *via* the conduction d-electrons has been established [3]. Due to the high absorption cross section of Gd (49700 barn for 2200 m/s neutrons), there have been no detailed neutron scattering investigations of GdS. In [5] a magnetic structure determination by neutron powder diffraction at 4.2 K has been reported. The authors found antiferromagnetic order of the second kind in the fcc lattice. In this type of order, the spins are parallel within (111) planes, which are stacked in an alternating antiparallel sequence along the [111] direction. Unfortunately, neither a diffraction pattern, nor a table of observed intensities is given in [5]. However, the authors claim that the moments lie within the (111) planes. Hulliger and Siegrist [4] performed a detailed investigation of the low-temperature phase transitions in GdS. Combining X-ray diffraction and susceptibility measurements, they found up to three different phases in the magnetically ordered regime. The structural distortions are attributed to type II antiferromagnetic order with different orientations of the magnetic moments: a truly trigonal phase, where the cubic unit cell is rhombohedrally elongated along [111] with the magnetic moments pointing in the [111] direction, a monoclinic phase, where the moments point in [110] directions, and a monoclinic phase, which is pseudo rhombohedrally squeezed along [111], for which the spins are in the (111) planes. The authors found that the exchange interactions are very sensitive to the stoichiometry and to defects, which modify the lattice constants and the electron concentration. Therefore, different samples exhibit different phases. The low-temperature phase transitions were attributed to spin flips, which can be accounted for by a model including anisotropic exchange interactions. It should also be noted that below the Néel temperature, a very pronounced field dependence of the susceptibility has been observed in all the phases studied. Very recent measurements [6] indicate that besides the bilinear exchange interactions discussed above, fourth-order exchange interactions (biquadratic and three-spin exchange) are relevant for this compound.

The wealth of low-temperature phenomena reported on this compound is surprising for such a system, which we expect to be Heisenberg-like from simple arguments. So far, the evidence for the various low-temperature magnetic structures has been very indirect (magnetization measurements and X-ray diffraction). Due to the difficulty to perform neutron diffraction experiments on these compounds [5], we decided to reinvestigate the magnetic structure of GdS employing a new technique, namely magnetic X-ray scattering. While non-resonant magnetic X-ray diffraction is a very small effect compared to charge scattering, large resonance enhancements are observed at the rare-earth $\mathrm{L_{II}}$ and $\mathrm{L_{III}}$ edges, *e.g.* in holmium [7], and have been subsequently explained as resulting from electric multipole transitions with the sensitivity to the magnetization arising from exchange [8]. Resonance exchange scattering (XRES) is a process described in second-order perturbation theory and can provide spectroscopic information about the density of states above the Fermi energy, in addition to providing information about the arrangement of the magnetic moments on an atomic scale. It is, however, not related in a simple and direct way to the sublattice magnetization, even so, under certain conditions, such a relation can be established [9]. Besides the information on the magnetism of GdS, our paper deals with methodological aspects of XRES. By comparing to neutron diffraction, we show that the intensity in our XRES experiment is indeed related to the square of the magnitude of the sublattice magnetization. Using polarisation analysis, we were able to identify the relevant virtual transitions in the XRES process. A careful absorption correction allowed us to analyse the shape of the resonance curve and explain its asymmetry. We apply the method to obtain information about the magnetic structure of GdS, the temperature dependence of the sublattice magnetization and of the lattice distortions, and finally about the critical behaviour close to the phase transition. A similar, but less detailed, study has been performed on GdSe with somewhat different results [10], which will be discussed.

2 X-ray resonance exchange scattering

In addition to non-resonant X-ray magnetic scattering discussed *e.g.* by Blume [11] and Blume and Gibbs [12], resonance phenomena occur if the X-ray energy is tuned to the absorption edges of magnetic elements. In the non-relativistic treatment introduced in [11,12], these resonances are described in second-order perturbation theory [8,13]. Electric multipole (predominantly dipole and quadrupole) operators induce virtual transitions between core levels and unoccupied states above the Fermi energy. These processes become sensitive to the magnetic state due to the difference in occupation of minority and majority bands leading to resonance exchange scattering. Intensity gain factors of typically two orders of magnitude are observed for the lanthanide $\mathrm{L_{II}}$ and $\mathrm{L_{III}}$ edges [7]. At the M_{IV} edge of actinides, this intensity gain can be as high as seven orders of magnitude [14].

Close to the absorption edges, the elastic cross section for scattering of photons with incident polarisation ε into a state of final polarisation ε' can be written as

$$\left.\frac{\mathrm{d}\sigma}{\mathrm{d}\Omega}\right|_{\varepsilon\to\varepsilon'} = \left[\frac{e^2}{mc^2}\right]^2 \left|\langle f_{\mathrm{C}}\rangle_{\varepsilon'\varepsilon} + \mathrm{i}\frac{\lambda_{\mathrm{c}}}{d}\langle f_{\mathrm{M}}\rangle_{\varepsilon'\varepsilon} + \langle f_{\mathrm{R}}\rangle_{\varepsilon'\varepsilon}\right|^2 . \tag{1}$$

Here $r_{\mathrm{e}} = \frac{e^2}{mc^2} \approx 2.818$ fm denotes the classical electron radius, $\lambda_{\mathrm{c}} = \frac{h}{mc} = 2.426$ pm the Compton length of an electron and d the lattice d-spacing. The scattering amplitudes $\langle f_{\mathrm{C}}\rangle$, $\langle f_{\mathrm{M}}\rangle$ and $\langle f_{\mathrm{R}}\rangle$, which describe the polarisation dependencies of charge, magnetic and resonant scattering, respectively, are given as matrices. Here, we discuss the case of linear polarisation, described by unit vectors perpendicular to the wave vectors of incident and scattered photons $\mathbf{k}$ and $\mathbf{k}'$. σ polarisation corresponds to the basis vector perpendicular to the scattering plane, π polarisation corresponds to a vector in the $\mathbf{k}$, $\mathbf{k}'$ plane. The basis vectors employed here and the expression for charge and non-resonant magnetic scattering are given in [15]. The energy dependent amplitude f_{R} reads in dipole approximation:

$$f_{\mathrm{R}}^{E_1}(E) = f_0(E) + f_{\mathrm{circ}}(E) + f_{\mathrm{lin}}(E) \tag{2}$$

with

$$\begin{aligned} f_0(E) &= (\boldsymbol{\varepsilon}'\boldsymbol{\varepsilon})\left[F_{+1}^1 + F_{-1}^1\right] \\ f_{\mathrm{circ}}(E) &= \mathrm{i}(\boldsymbol{\varepsilon}' \times \boldsymbol{\varepsilon})\mathbf{m}\left[F_{-1}^1 - F_{+1}^1\right] \\ f_{\mathrm{lin}}(E) &= (\boldsymbol{\varepsilon}'\mathbf{m})(\boldsymbol{\varepsilon}\,\mathbf{m})\left[2F_0^1 - F_{+1}^1 - F_{-1}^1\right] . \end{aligned} \tag{3}$$

f_0 is independent of the magnetic state (*i.e.* the conventional anomalous charge scattering), while f_{circ} and f_{lin} are the amplitudes connected for the special case of forward scattering with circular and linear dichroism, respectively. All three amplitudes have different polarisation properties. f_{circ} depends in a linear fashion on the direction of the magnetic moment $\mathbf{m}$, while f_{lin} depends quadraticly on $\mathbf{m}$. Therefore, for antiferromagnets, only f_{circ} gives a contribution at positions in reciprocal space separated from the main charge reflections by the magnetic propagation vector. f_{lin} can contribute to additional higher-order satellites. Finally, for a simple one-level excitation, the energy dependence of the amplitudes is contained in the oscillator strength

$$F_{\mathrm{M}}^1(E) = \frac{\alpha_{\mathrm{M}}/E}{(E - E_0) - \mathrm{i}\Gamma/2} . \tag{4}$$

Here E denotes the photon energy, E_0 the position of the absorption edge and Γ the resonance width. The phenomenological parameter α_{M} gives a measure of the amplitude of the resonance and represents the product of the transition matrix elements.

The expression for the quadrupolar amplitude $f_R^{E_2}(E)$ is very lengthy and will not be reproduced here. We refer to [13] and [16]. Because it is of relevance for the interpretation of our polarisation-analysis experiments, we just quote the result that for electric quadrupolar transitions, $\sigma \to \sigma$ scattering can occur at the positions of the magnetic superstructure reflections, while according to (3) $\sigma \to \sigma$ scattering is forbidden for f_{circ} at the magnetic Bragg positions. Due to this different polarisation dependence, XRES from dipole transitions can be clearly distinguished from anomalous charge scattering (3) and from XRES involving electric quadrupolar transitions.

3 Experimental

Samples of GdS were prepared by mineralization as described in detail in [17]. The powdered compounds, obtained from a primary reaction, were pressed into pellets, which were encapsulated in tungsten crucibles and heated for three weeks at a temperature about 50 °C below the melting temperature. Single crystals of very high quality with a mosaic spread of a few hundredths of a degree were prepared with a slight sulphur excess. A microprobe analysis confirmed the very good homogeneity of the samples and gave a sulphur excess of 5%. From this analysis, the total amount of non-gadolinium and -sulphur constituents could be estimated to be less than 1%. From high-energy X-ray diffraction [18], we know that the sulphur excess forms precipitates of $\mathrm{GdS_2}$ growing concurrently on the (111) planes of GdS. While these precipitates can perturb macroscopic measurements, their diffraction effects are clearly separated from the GdS signal in reciprocal space. Therefore our results presented below are representative for pure stoichiometric GdS. Ingots prepared by mineralization had the shape of cylindrical rods. From this raw material, single crystals of typical dimensions $5 \times 4 \times 2$ mm^3 and bounded by (100) faces were prepared by cleaving. The faces had the typical golden shining metal colour. Care was taken not to expose these single crystals to air and humidity, which results in an oxidation process clearly visible by a change of colour.

Most magnetic X-ray scattering experiments reported here were performed on the wiggler beamline W1 of HASYLAB, Hamburg. The X-ray source is a multipole wiggler with a symmetric magnet structure of 16 periods and a critical energy of 8.1 keV at a gap of 34 mm. The X-ray beam is monochromatized by a water-cooled Si 111 double-crystal monochromator and focussed into the experimental station by a toroidal gold-coated mirror. The beam size at the sample position is in the order of 2×4 mm^2 (vertical × horizontal). With the DORIS III storage ring operating in five bunch mode at 4.5 GeV and 100 mA, a typical flux at the sample of 2×10^{11} photons/sec is obtained at a photon energy of 9 keV. As sample environment, we used a modified liquid He cryostat, which covers a temperature range from 1.8 to 300 K [19]. The scattered beam from the sample can be measured either with a Ge solid-state detector or an analyser setup as described in [20].

Additional experiments with polarisation analysis were performed at the magnetic scattering beam line (BL 12/ID 20) of the ESRF in Grenoble. Here, the X-ray source was a planar undulator and the beam is tailored *via* a two-mirror arrangement together with a liquid-nitrogen-cooled Si 111 double-crystal monochromator. The sample was mounted in a closed-cycle refrigerator. A temperature range of 10 to 300 K could be covered in four-circle geometry. For polarisation analysis, a pyrolytic graphite crystal was employed, which has a diffraction angle $2\,\theta$ close to 90° for the gadolinium $\mathrm{L_{II}}$ and $\mathrm{L_{III}}$ edges.

To confirm the temperature dependence of the sublattice magnetisation and the magnetic structure deduced from the X-ray experiment, and to determine the total ordered moment, we carried out a neutron diffraction experiment on a single crystal of dimensions $3.0 \times 1.3 \times 1.2$ mm^3 at the high-flux reactor of the Institute Laue-Langevin, Grenoble. Since the absorption cross section of Gd amounts to roughly 40 kbarns for thermal neutrons, we performed this experiment with hot neutrons of wavelength 0.47 Å on the four-circle diffractometer, D9, employing a position sensitive area detector. At this

Table 1. Comparison of magnetic structure models for different spin orientations. The first lines give the XRES results measured at 4 K, together with the refined values for the q-domain population. The last line compares the agreement indicator χ^2 for the 49 magnetic reflections measured with neutron diffraction at $T = 15$ K for the four models. The meaning of the symbols is as follows:
2θ: diffraction angle; α: angle of incidence to (100) plane;
$|F_{\rm obs}|^2$: magnitude squared of the observed structure factor at 4 K and for 7931 eV;
σ: estimated standard deviation for $|F_{\rm obs}|^2$;
$|F_{\rm cal}^{hkl}|^2$: magnitude squared of the calculated structure factor for $\mathbf{m} \parallel (hkl)$.

$h\ k\ l$	2θ	α	$\lvert F_{\rm obs}\rvert^2$	σ	$\lvert F_{\rm cal}^{111}\rvert^2$	$\lvert F_{\rm cal}^{2\bar{1}\bar{1}}\rvert^2$	$\lvert F_{\rm cal}^{011}\rvert^2$	$\lvert F_{\rm cal}^{100}\rvert^2$
$\frac{5}{2}\frac{\bar{1}}{2}\frac{\bar{1}}{2}$	42.9	37.3	664	30	727	180	683	383
$\frac{7}{2}\frac{\bar{1}}{2}\frac{\bar{1}}{2}$	60.4	41.6	1512	38	1740	1092	1825	1441
$\frac{9}{2}\frac{\bar{1}}{2}\frac{\bar{1}}{2}$	79.8	48.8	242	18	205	348	371	380
$\frac{9}{2}\frac{1}{2}\frac{1}{2}$	79.8	31.0	1447	36	53	1642	922	1434
$\frac{11}{2}\frac{1}{2}\frac{1}{2}$	102.7	44.0	454	18	6	411	252	378
$\frac{11}{2}\frac{3}{2}\frac{3}{2}$	112.2	35.0	1308	44	729	1406	1275	1423
q-domain population ([111]:[$\bar{1}$1 1])					4:1	4:1	3.6:1	3.8:1
χ^2 for the neutron refinement					602	2.32	160	37.9

wavelength, the absorption cross section of Gd is roughly 500 barns. Second-order wavelength contamination of the incident beam was suppressed by an In filter. The sample temperature was maintained by an Air Products Displex cryorefrigerator.

4 Experimental results

4.1 Magnetic structure and energy dependence of resonance exchange scattering

As discussed in the introduction, we expect the gadolinium ions of GdS to exhibit antiferromagnetic order of the second kind in the fcc lattice. Therefore, we searched for magnetic Bragg reflections of type $\frac{2n+1}{2}, \frac{2n'+1}{2}, \frac{2n''+1}{2}$. Indeed, a strongly temperature-dependent Bragg signal was found at the reciprocal lattice positions given in Table 1. The signal vanishes above a temperature of 58 K, which has been identified in susceptibility measurements as the Néel temperature for this compound [6]. To exclude the existence of further magnetic Bragg reflections, linear scans were conducted in reciprocal space along the main symmetry directions. As the result of this search, only Bragg reflections characteristic of type-II antiferromagnetic order were found. To verify further the magnetic nature of the observed signal, rocking-curve scans were performed as a function of energy close to the $\mathrm{L_I}$, $\mathrm{L_{II}}$ and $\mathrm{L_{III}}$ absorption edges of gadolinium. At the $\mathrm{L_I}$ absorption edge, the magnetic signal is extremely difficult to observe and we were not able to detect any resonance behaviour. For the energy scans at the $\mathrm{L_{II}}$ and $\mathrm{L_{III}}$ absorption edges, a Ge detector with an energy resolution of 250 eV was employed. This enabled us to separate the elastic signal from fluorescence scattering and to resolve the structure of the fluorescence lines. Figure 1 shows energy spectra of the fluorescence signal in the vicinity of the $\mathrm{L_{II}}$ and $\mathrm{L_{III}}$ edges. In these scans, the elastic background is negligible compared to the fluorescence signal. During energy scans at the $\mathrm{L_{III}}$ absorption edge, it is mainly the L_α component that changes in intensity, while this component stays constant around the $\mathrm{L_{II}}$ absorption edge. At the $\mathrm{L_{II}}$ edge, the dominant component is the $\mathrm{L}_{\beta 1}$ fluorescence. As a consequence of these observations, the energy dependence of the absorption at the $\mathrm{L_{II}}$ and $\mathrm{L_{III}}$ edges was monitored through the signal of the $\mathrm{L}_{\beta 1}$ and L_α fluorescence lines, respectively. From the fluorescence signal, the energy dependence of the mass-absorption coefficient can be deduced as detailed in Appendix A. This mass-absorption coefficient was used to correct the Bragg signal as a function of energy. Note that a reliable absorption correction is essential to obtain the correct shape of the resonance line and the correct branching ratios, *i.e.* the ratio between the resonance enhancements at the $\mathrm{L_{II}}$ and $\mathrm{L_{III}}$ absorption edges. The absorption correction is non-trivial due to the strong energy dependence of the mass-absorption coefficient within the white line. However, we have carefully cross-checked our absorption corrections and are confident of the results. Figure 2a and b show the resonance behaviour of the Bragg signal obtained at the $\frac{9}{2}\frac{1}{2}\frac{1}{2}$ position

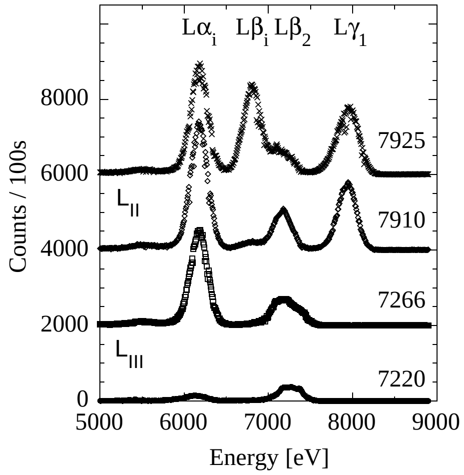

Fig. 1. Energy spectra of the fluorescence signal in the vicinity of the L_{II} and L_{III} absorption edges. For clarity, the scans at different energies have been displaced vertically by a constant amount.

for the L_{II} and L_{III} absorption edges, respectively. The data are corrected for absorption, which does not completely remove the asymmetry of the resonance line shape obtained in the raw data. As can be seen in Figure 2, the high energy wings of the corrected resonance curves are clearly suppressed as compared to the low energy wings. This asymmetry can be attributed to an interference between resonant and non-resonant magnetic scattering. If we follow references [8] and [13], the cross section can be written in the form

$$\frac{\mathrm{d}\sigma}{\mathrm{d}\Omega} \sim \left| A_{\mathrm{c}} + \mathrm{i}\left(A_{\mathrm{M}} + \frac{A_{\mathrm{R}}}{E}\frac{1}{(E-E_0)+\mathrm{i}\dfrac{\Gamma}{2}} \right) \right|^2 \qquad (5)$$

with obvious abbreviations A_{C}, A_{M} and A_{R} for the amplitudes. If we assume that charge scattering (resonant or non-resonant) is negligible at the position of the magnetic Bragg reflections and that A_{M} and A_{R} are real (second term of equation (10) of reference [13]), then the cross section assumes the following form:

$$\frac{\mathrm{d}\sigma}{\mathrm{d}\Omega} \sim A_{\mathrm{M}}^2 + \frac{A_{\mathrm{R}}^2}{E^2}\frac{1}{(E-E_0)^2+\left(\dfrac{\Gamma}{2}\right)^2} + 2A_{\mathrm{M}}\frac{A_{\mathrm{R}}}{E}\frac{E-E_0}{(E-E_0)^2+\left(\dfrac{\Gamma}{2}\right)^2}\,. \qquad (6)$$

This functional form of the cross-section has been fitted to the absorption-corrected resonance curves plotted in Figure 2. A convolution with the experimental energy resolution of the monochromator (about 4 eV) has been taken into account. The results of the refinements are given in Table 2. At both edges, the resonance energy coincides within the estimated standard deviations (ESD) with the arithmetic average between the energy of the absorption edge and the energy of the white line. The resonance level width at the two edges is comparable since the ESD given in Table 2 does not take into account the uncertainties in the energy resolution of the monochromator. The average level width of 2.5 eV corresponds to a lifetime of the exited state of 0.26 fs, according to the Heisenberg uncertainty relation. The branching ratio, *i.e.* the ratio between the absorption corrected maximum resonance intensity at the L_{II}- and L_{III}-edge is approximately 2.5. The resonance enhancement at the L_{III}-edge, *i.e.* the ratio between the maximum intensity in resonance and the intensity for non-resonant magnetic scattering, is of the order of 100.

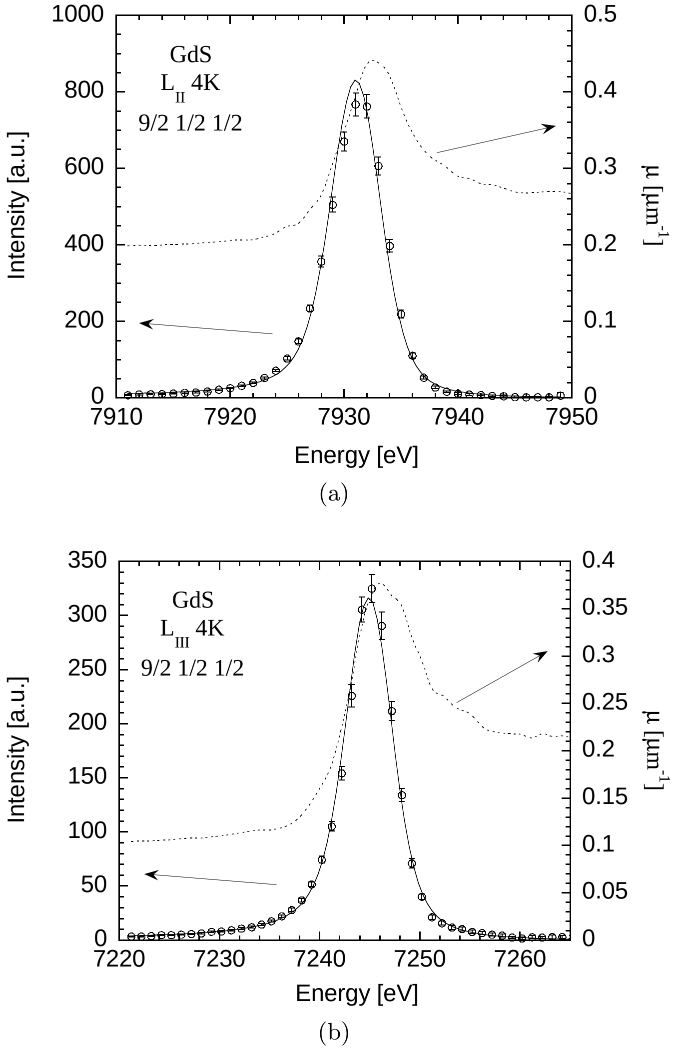

(a)

(b)

Fig. 2. (a) Integrated intensity *versus* energy for the 9/2 1/2 1/2 magnetic Bragg reflection close to the L_{II} absorption edge. The temperature was 4 K. The solid line shows the result of a refinement as described in the text. The dashed line shows the linear absorption coefficient, which we obtained from measurements of the fluorescence yield. (b) Same as Figure 2a but at the L_{III} edge.

Table 2. Spectroscopic data for the resonance behaviour of GdS at the $\frac{9}{2}\frac{1}{2}\frac{1}{2}$ magnetic Bragg reflection at 2 K. The meaning of the symbols is as follows:
E_{E}: Absorption-edge energy (point of inflection; normalised to tabulated values);
E_{WL}: White-line energy (absorption maximum);
E_{O}: Resonance energy (compare (4));
Γ: Resonance-level width (compare (4));
$I_{\max}$: Maximum intensity in resonance.

Edge	E_{E} [eV]	E_{WL} [eV]	E_{O} [eV]	Γ [eV]	$I_{\max}$ [a.u.]	Resonance enhancement
$\mathrm{L_{II}}$	7930.0(8)	7932.0(6)	7931.1(1)	2.2(2)	820(45)	270
$\mathrm{L_{III}}$	7243.0(5)	7246.2(7)	7245.0(1)	2.8(2)	315(11)	105

4.2 Polarisation analysis of resonance exchange scattering

In order to determine whether dipolar or quadrupolar transitions are involved in the resonance behaviour, we performed polarisation-analysis experiments at beamline ID 20 of the ESRF. A pyrolytic graphite crystal with a mosaic width of about 0.3 degree has been employed. For this crystal, the 006 Bragg reflection is diffracted at an angle of 87 degrees at the energy of the Gd-$\mathrm{L_{II}}$-resonance. The crystal acts as nearly perfect polarisation analyser, since the polarisation factor for π-π-scattering amounts to less than 3% of the polarisation factor of σ-σ-scattering at this angle. Moreover, since the mosaic spread of the analyser is large compared to the horizontal and vertical divergences of the undulator radiation, the total scattered intensity can easily be collected. Since, in addition, the polarisation of the incident beam was larger than 99.5%, we could neglect all corrections due to the finite incident polarisation and the finite efficiency of the polarisation analyser. Figure 3 shows polarisation-analysis scans of the $\frac{5}{2}\frac{1}{2}\frac{1}{2}$ Bragg peak at 20 K. In resonance at 7931 eV, the scattering is nearly exclusively $\sigma \rightarrow \pi$. However, in the pre-edge region about 5 eV below the resonance, we could also observe a signal in the $\sigma \rightarrow \sigma$ polarisation channel, see Figure 3b. The temperature dependence of this resonance suggests its magnetic nature. According to Section 2, this indicates that the dominant resonance effect is due to dipolar transitions from the $2p$-states to the $5d$ conduction electron band. However, at about 7926 eV, a small quadrupolar resonance for transitions from the $2p$ to the $4f$ states can be observed. The quadrupolar resonance enhancement is about a factor 300 smaller than the dipolar one. Table 3 gives the polarisation dependence of several other reflections. In all cases, the $\sigma \rightarrow \pi$ channel is clearly dominant.

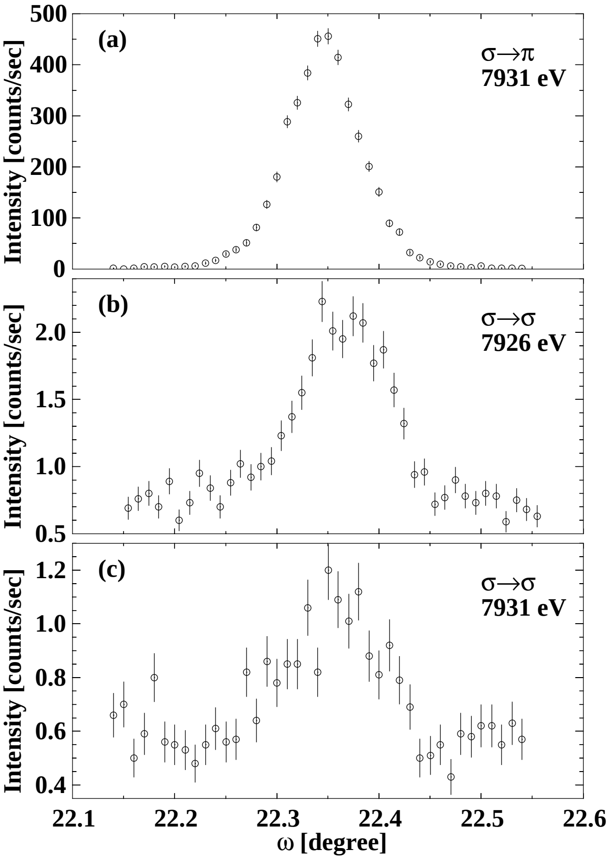

Fig. 3. Polarisation analysis scans of the $\frac{5}{2}\frac{1}{2}\frac{1}{2}$ peak of GdS at 20 K. (a) $\sigma \rightarrow \pi$ channel at 7931 eV ($\approx \mathrm{L_{II}}$ edge); (b) $\sigma \rightarrow \sigma$ channel at 7926 eV (below edge); (c) $\sigma \rightarrow \sigma$ channel at 7931 eV.

4.3 Temperature dependence of the sublattice magnetization

The temperature dependence of the magnetic $\frac{9}{2}\frac{1}{2}\frac{1}{2}$ reflection has been measured in resonance at the $\mathrm{L_{II}}$-edge (7931 eV). We assume the sublattice magnetization to be proportional to the square root of the integrated intensity of the magnetic Bragg reflections. This assumption is non-trivial since resonance exchange scattering is a second-order process and not directly related to simple thermodynamic quantities such as the sublattice magnetization (compare however [9]). To verify this assumption for our case of GdS, we have performed an additional neutron diffraction experiment. In the insert of Figure 4, we compare the temperature dependence obtained with X-ray resonance exchange scattering and neutron diffraction. The temperature dependence is strictly identical, which shows that with XRES, we have a measure of the sublattice magnetization for GdS. This sublattice magnetization follows very nicely a mean-field function for spin $S = \frac{7}{2}$

Table 3. Polarisation analysis of magnetic Bragg scattering from GdS at 16 K in resonance at the L_{II} edge. The tabulated values are observed intensities in arbitrary units, corrected for absorption and Lorentz-factor ($|F_{\mathrm{obs}}|^2$).

Reflection	Bragg-Angle	$\sigma \rightarrow \sigma$ 7926 eV	$\sigma \rightarrow \pi$ 7931 eV
$\left(\frac{3}{2}\frac{1}{2}\frac{1}{2}\right)$	13.49	0.0002	0.1026
$\left(\frac{5}{2}\frac{1}{2}\frac{1}{2}\right)$	21.44	0.0005	0.1314
$\left(\frac{7}{2}\frac{1}{2}\frac{1}{2}\right)$	30.15	0.0011	0.3219
$\left(\frac{9}{2}\frac{1}{2}\frac{1}{2}\right)$	39.85	0.0024	0.3292
$\left(\frac{11}{2}\frac{1}{2}\frac{1}{2}\right)$	51.27	–	0.4019

as is plotted in Figure 4. In order to determine the critical behaviour close to the phase transition, we have taken many more data points in the X-ray experiment for temperatures between 55 and 60 K. The result is plotted in Figure 5. The inset shows the temperature variation of the integrated intensity as obtained from a fit assuming a Gaussian line shape (full diamonds) and from a simple summation of the intensity over the scan range with background correction (open circles). Below 57.6 K, the two methods give identical results. Above 57.6 K, a Gaussian fit is no longer appropriate, since a line broadening is observed indicating the presence of magnetic critical diffuse scattering. However, the statistical quality of the data was not sufficient to separate clearly the Bragg and the diffuse components in this temperature range. Therefore, data very close to the Néel temperature had to be excluded from the determination of the critical exponent. Figure 5 shows the remaining data of the reduced sublattice magnetization *versus* reduced temperature in a double logarithmic plot. The straight line corresponds to an exponent of $\beta = 0.378(20)$ in the expression $m \sim \tau^{\beta}$ with $m = M/M_{\mathrm{s}}$, $\tau = \frac{T_{\mathrm{N}} - T}{T_{\mathrm{N}}}$. Here M, M_{s} and T_{N} denote the sublattice magnetization, the saturation value of the sublattice magnetization and the Néel temperature, respectively. The Néel temperature was determined from this refinement to be $T_{\mathrm{N}} = 57.72(3)$ K. For $\tau > 0.06$, the data deviate from the power law. These data were excluded from the fit.

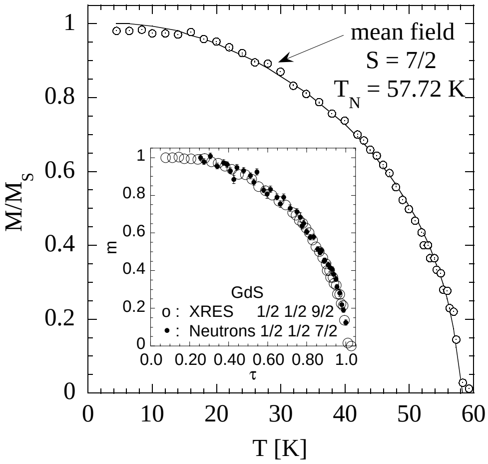

Fig. 4. Reduced sublattice magnetization *versus* temperature. The open circles show the temperature dependence of the square root of the integrated intensity of the 9/2 1/2 1/2 reflection in the L_{II} resonance, normalized to its saturation value. The solid line represents mean-field behaviour for $S = 7/2$ and $T_{\mathrm{N}} = 57.72$ K. Inset: Comparison of XRES and neutron data in reduced coordinates for the sublattice magnetization $m = M/M_{\mathrm{s}}$ and the reduced temperature $\tau = T/T_{\mathrm{N}}$.

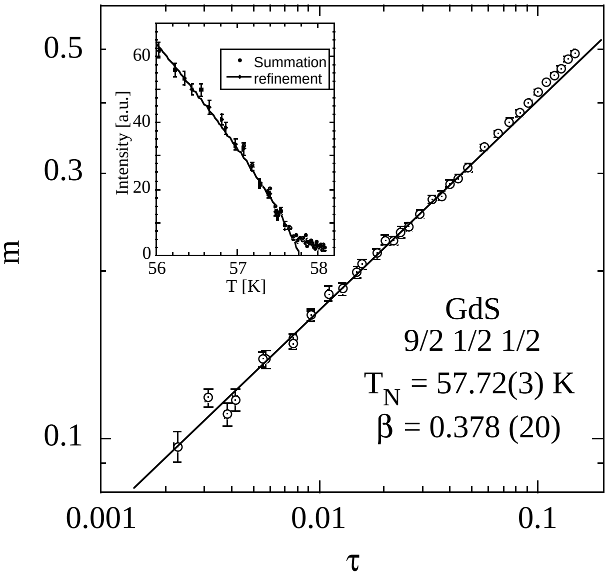

Fig. 5. Critical behaviour of the sublattice magnetization in a double logarithmic plot. m and τ denote the reduced values of the sublattice magnetization and temperature as defined in the text. The solid line is a refinement with a power law. The inset shows the integrated intensity *versus* temperature close to the phase transition, see text.

The measurements of the temperature dependence reported so far have been performed without an analyser crystal, *i.e.* the Bragg diffracted signal from the GdS sample was measured with a detector of sufficient aperture to insure proper integration for each point in a rocking curve scan. In an effort to investigate the critical behaviour in more detail, we performed additional experiments at beamline ID 20 of the ESRF using a silicon 111 analyser in the scattered beam in order to improve the reciprocal space resolution. Our hope was that with the improved momentum space resolution, the Bragg signal could be better separated from magnetic diffuse scattering. During these measurements, we discovered that even well above the Néel temperature a non-vanishing resolution-limited signal was observable at the position of magnetic Bragg reflections $\frac{5}{2}\frac{\bar{1}}{2}\frac{\bar{1}}{2}$, $\frac{7}{2}\frac{\bar{1}}{2}\frac{\bar{1}}{2}$, $\frac{9}{2}\frac{\bar{1}}{2}\frac{\bar{1}}{2}$, $\frac{5}{2}\frac{1}{2}\frac{1}{2}$, $\frac{7}{2}\frac{1}{2}\frac{1}{2}$, $\frac{9}{2}\frac{1}{2}\frac{1}{2}$. This intensity is essentially temperature independent (up to 200 K, the limit of our measurement). It shows no resonance at

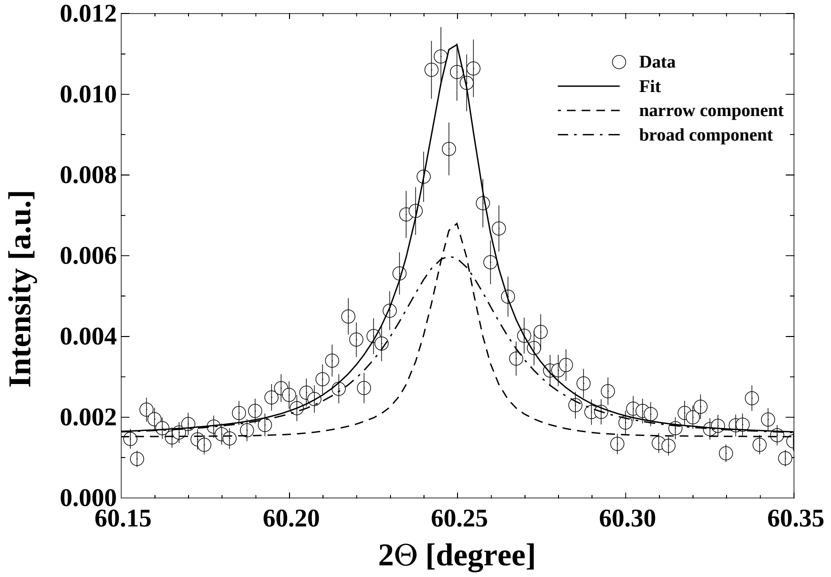

Fig. 6. Longitudinal scan ($\theta - 2\ \theta$) at the $\frac{7}{2}\frac{1}{2}\frac{1}{2}$ position for a temperature of 57.3 K, 0.27 K above T_N. The solid line shows a fit of a broad Lorentzian and a sharp Lorentzian-squared component, compare dot-dashed and dashed lines, respectively. Both components were convoluted with the instrumental resolution function.

the Gd L edges and its intensity is comparable with the non-resonant magnetic intensity in the limit $T \rightarrow 0$. A possible explanation for this signal is a weak remaining $\lambda/2$-contribution from charge reflections. In order to obtain the true XRES signal, we have calculated a difference signal to the high temperature data. With a procedure similar to the one described above, a critical exponent of $\beta = 0.384(5)$ was determined. Again, due to the limited statistical accuracy of our data, a clear separation of Bragg and magnetic diffuse scattering turned out to be difficult. We were not able to determine the critical exponents γ and ν for susceptibility and correlation length, respectively. However, we observed that above the Néel temperature, the magnetic signal could not be described by a one-component line shape alone. This is depicted in Figure 6, which shows a longitudinal scan at the $\frac{7}{2}\frac{1}{2}\frac{1}{2}$ position of the GdS crystal 0.27 K above the Néel temperature. The data could only be fitted by assuming a two-component line shape with a sharp component having the width and shape of the low temperature Bragg signal remaining even above T_N.

4.4 Temperature dependence of the lattice

Figure 7a and b show the temperature dependence of the full width-half maximum (FWHM) and the position of the magnetic $\frac{9}{2}\frac{1}{2}\frac{1}{2}$ and the charge 400 Bragg reflection. Measurements at the 400 have been performed up to 80 K. Between 80 K and 52 K, the lattice shrinks with a linear temperature dependence. No anomaly can be detected at the Néel temperature. At temperatures below 20 K, the crystal lattice remains essentially temperature independent. However, two clear anomalies can be seen in both the position and in the width of the charge and magnetic reflections at 32 K and 49 K. The measurements shown in Figure 7 have been made with medium resolution on beamline W1 at HASYLAB. With this resolution (about 10^{-3} Å^{-1}) a splitting of the $\frac{9}{2}\frac{1}{2}\frac{1}{2}$ Bragg reflection could not be detected. However, the temperature dependence of the peak width suggests that such a splitting is indeed present. We have performed additional scans with higher resolution employing a silicon 111 analyser at the beamline ID 20 of the ESRF at the magnetic $\frac{5}{2}\frac{1}{2}\frac{1}{2}$, $\frac{11}{2}\frac{1}{2}\frac{1}{2}$ and the charge 511 reflections. Figure 8 shows a series of rocking curve scans performed on the $\frac{11}{2}\frac{1}{2}\frac{1}{2}$ reflection for temperatures between 60 and 20 K. It can be clearly seen that the peak splits in an intermediate temperature range between 32 ± 2 and 47 ± 2 K. This splitting is more obvious in the contour plot in Figure 9. Its elongated shape is due to the mosaic width of 0.09 degrees. At 40 K, this peak splits along the $\left[1\bar{1}0\right]$ direction. The splitting amounts to about 0.03 degree.

4.5 Direction of the magnetic moment

In Table 1, the observed magnetic Bragg reflections are given. They were all measured at a photon energy of 7931 eV ($\mathrm{L_{II}}$ resonance). For all reflections, the plane of diffraction was the $\left(01\bar{1}\right)$ plane. Integrated intensities have been determined from rocking curve scans. They were corrected for the Lorentz factor and absorption according to

$$|F_\mathrm{obs}|^2 = \sin 2\theta \left(1 + \frac{\sin\alpha}{\sin\beta}\right) I_\mathrm{obs}. \tag{7}$$

Here, F_obs denotes the magnetic structure factor in the arbitrary units of the measurement, I_obs the measured integrated intensity, 2θ the diffraction angle and α and β the angles between the cleaved (100) face of the crystal and the incident and diffracted beams, respectively.

$$F_{\mathrm{cal}} = \sum_j m'_j \,\mathrm{e}^{\mathrm{i}\mathbf{Q}\cdot\mathbf{r}_j} = \begin{cases} 8m' \left[1 - (-1)^{\frac{h+k}{2}} - (-1)^{\frac{h+l}{2}} - (-1)^{\frac{k+l}{2}} \right] & \text{for } h,k,l = \dfrac{2n+1}{2}, \dfrac{2n'+1}{2}, \dfrac{2n''+1}{2} \\ 0 & \text{otherwise.} \end{cases} \tag{8}$$

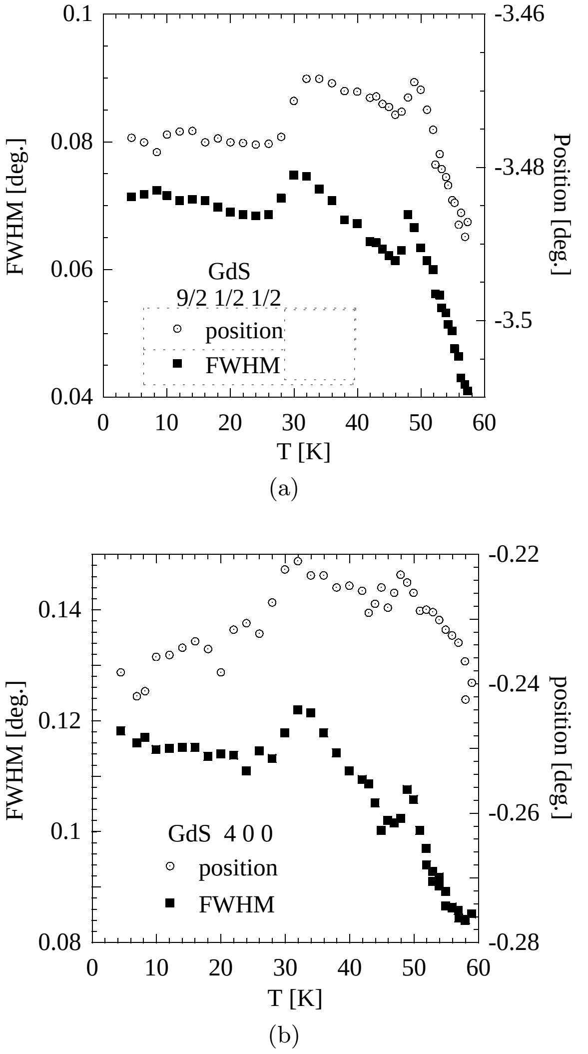

(a)

(b)

Fig. 7. (a) Full width at half maximum and position of the magnetic 9/2 1/2 1/2 peak as a function of temperature. (b) The same for the charge 400 reflection.

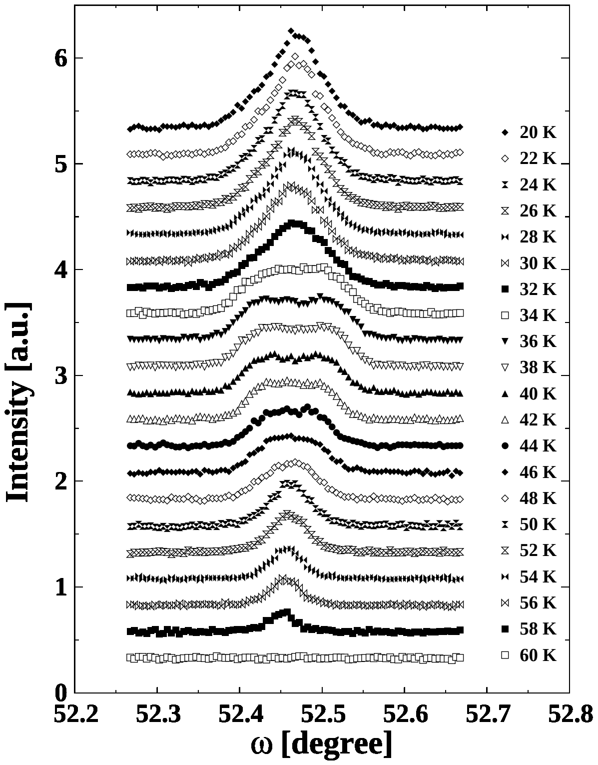

Fig. 8. Series of rocking curve scans of the $\frac{11}{2}\frac{1}{2}\frac{1}{2}$ peak for temperatures between 60 K and 20 K. For clarity, the scans have been displaced vertically by a constant amount.

During the measurements, the beam polarisation was approximately 94%. Given this high degree of polarisation, we neglected any polarisation factor. Since the beam size was small compared to the crystal dimensions, we also neglected any geometrical factors. This might be a crude approximation since the beam was certainly not homogenous and will lead to systematic errors in the observed structure factor, which are expected to be several times the estimated standard deviation calculated on purely statistical grounds. The measured intensities were used to determine the direction of the magnetic moment in GdS, assuming a collinear spin structure. For an antiferromagnetic type-II structure, for which the moments in the (111) planes are parallel and successive planes are coupled antiferromagnetically, the magnetic structure factor, not including the Debye-Waller-factor, can be calculated as follows:

see equation (8) above

Here, the sum runs over all sites j within the magnetic unit cell, m'_j denotes the component of the sublattice magnetization vector visible in the diffraction experiment, $\mathbf{r}_j$ is the vector from the origin of the magnetic unit cell to the corresponding magnetic atom and $\mathbf{Q}$ is the scattering vector. From our polarisation analysis experiment, we know that the observed XRES signals are due to dipolar transitions. According to (3), the structure factor for $\sigma \to \pi$ dipolar transition is proportional to

$$F \sim (\boldsymbol{\varepsilon}' \times \boldsymbol{\varepsilon})\,\mathbf{m} = \hat{\mathbf{k}}'\,\mathbf{m} =: m' \tag{9}$$

i.e. in our experiments, we obtain information about the component of the sublattice magnetization parallel to the wave vector of the diffracted beam only.

Table 4. Magnetic neutron Bragg reflections of GdS at 15 K. F_{cal} is for a type-II antiferromagnetic with spins perpendicular to [111] and propagation vector 0.5 0.5 0.5.

h	k	l	F_{obs}	F_{cal}	h	k	l	F_{obs}	F_{cal}
2.5	0.5	0.5	117.8(0.8)	115.0	5.5	3.5	1.5	26.2(3.0)	27.7
4.5	0.5	0.5	60.0(0.7)	61.3	5.5	−0.5	3.5	29.4(2.0)	27.6
6.5	0.5	0.5	23.0(3.6)	26.5	5.5	−2.5	−0.5	30.1(2.0)	28.3
2.5	2.5	0.5	91.7(0.9)	93.3	5.5	1.5	−2.5	30.7(1.4)	27.7
2.5	0.5	−1.5	86.6(1.1)	86.4	2.5	2.5	2.5	79.6(3.2)	77.0
4.5	2.5	0.5	51.2(1.5)	52.1	2.5	−1.5	2.5	73.4(2.2)	72.4
4.5	0.5	−1.5	51.1(1.5)	50.5	2.5	−1.5	−1.5	75.1(1.1)	76.2
6.5	2.5	0.5	33.0(3.0)	22.5	4.5	2.5	2.5	43.8(1.7)	44.2
6.5	0.5	−1.5	21.7(2.8)	22.7	4.5	−1.5	2.5	39.9(1.8)	43.0
4.5	4.5	0.5	35.4(1.6)	31.3	4.5	−1.5	−1.5	42.9(2.6)	43.7
4.5	0.5	−3.5	30.4(2.2)	32.3	6.5	2.5	2.5	31.1(3.2)	19.1
6.5	0.5	−3.5	19.1(4.9)	14.7	6.5	−1.5	2.5	23.7(3.4)	19.3
1.5	1.5	1.5	129.1(1.0)	128.4	6.5	−1.5	−1.5	7.9(2.3)	19.9
1.5	−0.5	1.5	119.5(0.8)	119.5	4.5	4.5	2.5	24.6(2.5)	26.6
1.5	−0.5	−0.5	106.5(1.3)	111.4	4.5	−1.5	4.5	28.3(2.0)	26.5
3.5	1.5	1.5	82.3(2.4)	80.1	4.5	−3.5	−1.5	28.1(1.5)	29.6
3.5	−0.5	1.5	80.6(2.4)	77.4	4.5	2.5	−3.5	25.4(1.8)	26.9
3.5	−0.5	−0.5	77.5(1.0)	75.2	3.5	3.5	3.5	36.7(1.3)	38.9
5.5	1.5	1.5	39.9(1.0)	38.5	3.5	−2.5	3.5	36.8(1.3)	37.9
5.5	−0.5	1.5	38.5(1.2)	38.1	3.5	−2.5	−2.5	42.1(1.5)	43.7
5.5	−0.5	−0.5	39.2(1.0)	37.9	5.5	3.5	3.5	14.4(4.2)	19.8
3.5	3.5	1.5	54.1(2.3)	55.0	5.5	−2.5	3.5	14.3(3.7)	20.1
3.5	−0.5	3.5	52.8(1.0)	54.0	5.5	−2.5	−2.5	19.7(2.7)	22.1
3.5	−2.5	−0.5	53.9(1.3)	54.6	4.5	−3.5	−3.5	17.7(3.3)	21.0
3.5	1.5	−2.5	51.4(1.4)	52.8					

Within the resolution of the present experiment, GdS is still cubic at low temperatures. For such a highly symmetric structure, symmetry-equivalent domains have to be taken into account for the calculation of the structure factor. $\mathbf{q}$-domains for symmetric equivalent directions of the magnetic propagation vector $\mathbf{q}$ have to be considered, as well as S-domains for different spin orientations within a given $\mathbf{q}$-domain. Four $\mathbf{q}$-domains in total have to be distinguished: $\mathbf{q}$ parallel to the [111], [$\bar{1}11$], [$1\bar{1}1$] and [$11\bar{1}$] direction. The structure factors for the various $\mathbf{q}$-domains can be calculated from (8) by simply renaming the magnetic Bragg reflections. In our case of magnetic reflections of type $\frac{h}{2}\frac{k}{2}\frac{k}{2}$, only the [111] and the [$\bar{1}11$] domains are visible. For every $\mathbf{q}$-domain, we have to consider S-domains, if the spin does not lie in the direction of the magnetic propagation vector. These S-domains are due to the threefold [111] axis. While the $\mathbf{q}$-domains can be unequally populated due to internal strain, we assume that the S-domains are all equally populated and add up the corresponding intensity contributions. We end up with the following formula for the calculated structure factor averaged over the S-domains:

$$|F_{\mathrm{cal}}|^2 = S_{\mathbf{q}} \left[2 + \left(3\cos^2\delta - 1\right)\sin\varepsilon\left(\sin\varepsilon - 2\sqrt{2}\cos\varepsilon\right)\right]. \tag{10}$$

Here, $S_{\mathbf{q}}$ is a scaling factor for the corresponding $\mathbf{q}$-domain, δ is the polar angle between the magnetic moment and the magnetic propagation vector and ε is the angle between $\hat{\mathbf{k}}'$ and the [100] direction. In Table 1, calculated values of the squared structure-factor amplitude are given for four directions of the magnetic moment, *i.e.* the angle δ has been kept fixed, but the two scale factors for the $\mathbf{q}$-domains have been refined. As Table 1 shows, we find a rather unequal domain population, where the volume ratio of domains with propagation vector along [111] is about four times larger as compared to [$\bar{1}11$] domains. We attribute this to near-surface effects due to the limited penetration depth. There are distinct differences in the calculated values for the various models. Clearly the model where the magnetic moment is parallel to a [111] direction can be excluded. The differences between the other models are not so marked and significant deviations remain, which are partly due to our assumption of a homogenous beam and of equally populated S-domains. However, we want to stress the large differences in the calculated intensities for the $\frac{9}{2}\frac{1}{2}\frac{1}{2}$ reflection for the four spin models shown in Table 1. This reflection has been used to study the temperature dependence of the sublattice magnetization which showed a smooth meanfield type behaviour. If a spin reorientation occurred between T_{N} and 2 K, this should be visible as a large change of the measured intensity according to Table 1. Such an effect has not been observed, which indicates that the easy direction stays the same within all of the ordered phase of GdS.

With the few reflection observed and the rather large systematic errors due to geometrical factors, we cannot unambiguously determine the spin direction from the X-ray data. Moreover, resonance exchange scattering,

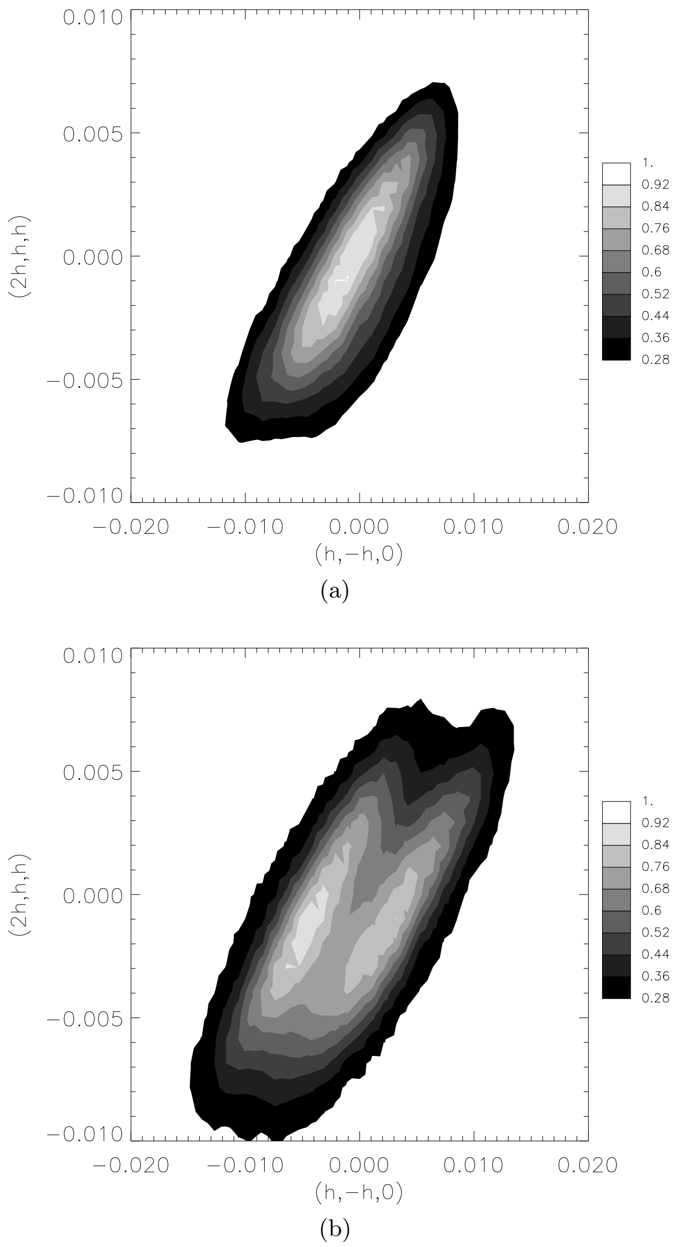

(a)

(b)

Fig. 9. Contour plot of the $\frac{11}{2}\frac{1}{2}\frac{1}{2}$ peak in the $(2h,\ h,\ h)$ and $(h,\ -h,\ 0)$ plane. The temperature was 20 K for Figure 9a and 40 K for Figure 9b.

as a second order perturbation process, does not allow us to determine the magnitude of the ordered magnetic moment. Therefore we carried out an additional neutron diffraction experiment at a temperature of $T = 15$ K. Various nuclear and magnetic reflections were scanned up to $\sin(\theta)/\lambda$ of 1.06 Å^{-1} and 0.65 Å^{-1}, respectively. After subtraction of the background following Wilkinson *et al.*, and correction for absorption by Gaussian integration (transmission range, 0.257–0.321), the data were averaged over equivalents to give 65 unique nuclear reflections and 49 unique magnetic reflections. The relative q-domain populations were 0.237 : 0.275 : 0.258 : 0.230. Due to the S-domain averaging, only the angle of the spin direction to the direction of propagation and the magnitude of the spin can be determined. Least-squares minimisation of the difference between the calculated and observed structure amplitudes gave best agreement for a model with the spin direction perpendicular to the direction of propagation (111) and a moment of 6.51(3) μ_B. This value was obtained in a joint refinement of the nuclear and magnetic reflections including refinement of the thermal displacement parameters of both Gd and S (0.15(1) and 0.11(1), respectively). Table 1 lists the values of the agreement indicator χ^2 for the 49 magnetic reflections alone for the directions considered in the analysis of the X-ray data. Table 4 lists the observed magnetic neutron scattering amplitudes and the calculated amplitudes of the best model.

5 Discussion

The experimental study presented in this paper has two main implications: one for the methodology of XRES and one for the study of the magnetism of GdS. Let us first discuss the implications for resonance-exchange scattering. XRES occurs at the absorption edges of the magnetic elements, where the absorption length changes drastically as the energy is tuned through the resonance. The correction of these absorption effects is an important prerequisite for a correct analysis of the resonance behaviour. The resonance occurs right at the absorption edge, where the detailed energy dependence of the absorption length depends critically on the chemical bonding. Therefore, we do not believe that absorption coefficients determined with a metallic Gd foil can be used for an absorption correction. To produce a GdS sample thin enough for an absorption measurement in transmission geometry is prohibitive due to the high risk of oxidation. Therefore, we decided to determine the energy dependence of the absorption on our single crystal sample itself *via* measurements of the fluorescence yield. In Appendix A, the formalism is detailed, which gives us the relation between fluorescence yield and absorption length. These detailed absorption corrections were necessary for an analysis of the resonance line shape. Using a polarisation-analysis setup, we were able to show that dipolar $2p \rightarrow 5d$ transitions are dominant at the $\mathrm{L_{II}}$ and $\mathrm{L_{III}}$ edges. Quadrupolar transitions occur a few eV below the dipolar transitions and are a factor of 300 weaker. This is in contrast to the observations in holmium, where large quadrupolar resonances were detected [7]. However, polarisation-analysis experiments in other rare-earth metals show that the situation in holmium is rather exceptional [21–28]. This in term implies that in our case of GdS, we do not probe the magnetism of the $4f$ levels directly, but instead only the induced moment in the $5d$ conduction band. As mentioned in the introduction, the induced moment in the conduction band is quite appreciable and amounts to some 0.3 μ_B as determined in the paramagnetic state from magnetization measurements.

Resonance-exchange scattering being a second-order perturbation process, is not connected in a simple way to the order parameter, the sublattice magnetization. However, for the so-called fast collision approximation, Luo *et al.* [9] were able to express the resonance amplitudes in terms of the experimentally significant quantities, the electron spin- and orbital moments. However, in our case, where the resonance line widths are rather small, it is not clear that the conditions of the fast-collision approximation hold. Moreover, changes in the crystal lattice occur below the Néel temperature, which might influence the structure of the $5d$ conduction band. Since our experiment is only sensitive to the magnetism of the $5d$ conduction band, we cannot be sure to measure the order parameter in a resonance-exchange scattering experiment. It is for this reason that we determined the temperature dependence of the sublattice magnetization independently using diffraction of hot neutrons. The excellent agreement between the neutron and the X-ray results (Fig. 4) gives us confidence that our resonance signal is indeed proportional to the square of the order parameter and that the total magnetic moment (as determined by neutron scattering) and the $5d$ moment (from XRES) have a similar temperature dependence. It is at first sight surprising that with XRES we found a temperature dependence characteristic for a $S = 7/2$ system: the X-ray experiment is sensitive to the $5d$ moment only and the $5d$ electrons are itinerant and do not correspond to $S = 7/2$. That a $S = 7/2$ behaviour has been measured confirms the very strong coupling of the $5d$ and $4f$ systems as required by RKKY theory.

Even after the absorption correction, the resonance line shapes as a function of energy remain asymmetric: the integrated intensities drop faster at the high energy side as compared to the low energy side. We were able to explain this effect partly with an interference of resonance exchange scattering and non-resonant magnetic scattering. However, our model does not reproduce the resonance line shapes in all detail. The deviations might be due to the detailed shape of the density of states of the unoccupied part of the conduction band. Our experimental resolution of about 4 eV is slightly larger than the average level width of 2.5 eV of the $\mathrm{L_{II}}$ and $\mathrm{L_{III}}$ resonances. According to [3], the width of the $5d$ conduction band is of the order of 4 eV and therefore comparable to our resolution. A crystal-field splitting of the $5d$ levels cannot be resolved with our experiment. Therefore, the detailed shape of the density of states will influence our measured line shapes. Here, an improved energy resolution of the beamline would certainly be desirable, however, the spectroscopic information obtainable with XRES is limited by the corehole lifetimes to some 2–3 eV. The level widths of 2.2 and 2.8 eV for the $\mathrm{L_{II}}$ and $\mathrm{L_{III}}$ edges, respectively, lie systematically below the semi-empirical values tabulated in [29]. These values are 4.0 eV at the Gd $\mathrm{L_{II}}$ edge and 4.3 eV at the $\mathrm{L_{III}}$ edge. However, newer experimental data [30] show that these semi-empirical values based on relativistic Hartree-Fock calculations systematically overestimate the line width. The experimental width measured on an atomic beam of Gd atoms are 3.0 (7) and 3.8 (7) eV for the $\mathrm{L_{II}}$ and $\mathrm{L_{III}}$ edge, respectively. The values we found are even smaller. We have to emphasis, however, that the estimated standard deviation of 0.2 eV given in Table 2 is based on a model assuming a pure Lorentzian line shape of the resonance. In addition, at the time of the experiment, the energy resolution of the monochromator of the beamline W1 depended on the current of the storage ring due to heatload effects. The 4 eV energy resolution of the monochromator, which we used for the convolution process, might therefore be an overestimate. These effects are difficult to quantify, but we expect our error bars to lie in the same order of magnitude as the values given in [30]. Within these uncertainties, our values for the line width and the values of [30] are in agreement. The position of the resonance midway between the inflection point of the absorption edge and the maximum absorption in the white line is consistent with observations on other rare-earths [21–28]. We found the absorption maximum about 1–2 eV above the edge. If the inflection point of $\mu(E)$ is identified with the Fermi energy, our observations are consistent with the energy level diagram given in [3], which shows the center of gravity of the $5d$ conduction band at about 1.5 eV above the Fermi level. As in the case of most rare-earth metals [21–28], no resonance could be observed at the $\mathrm{L_I}$ edge. This is not surprising since the overlap integral between the core $1s$ state and the $4f$ or $5d$ states is very small. However, the resonance effects at the $\mathrm{L_{II}}$ and $\mathrm{L_{III}}$ edges are remarkably large and amount to a factor of 100 or 300 in intensity compared to the non-resonant scattering. Finally, we want to point out the surprising value of 2.5 for the branching ratio of the resonance intensity at the $\mathrm{L_{II}}$ and $\mathrm{L_{III}}$ edges. Before absorption correction, this ratio amounts to 1.7. This should be compared with the data of GdSe [10]. There the intensity ratio in the uncorrected raw data was found to be 1.6, which is in agreement with our value. Since at the $\mathrm{L_{II}}$ edge the absorption is larger than at the $\mathrm{L_{III}}$ edge (compare Fig. 2a and 2b), the absorption-corrected value for the branching ratio has to be larger than 1.7, which holds in our case. For GdSe, the absorption-corrected branching ratio was quoted to be 1.3, but unfortunately the absorption coefficients are not listed. We would have expected that the absorption coefficients are similar for both compounds and with a larger absorption at the $\mathrm{L_{II}}$ edge, a branching ratio larger than 2 would result for GdSe also. Clearly, the branching ratio depends critically on the absorption correction, but for both compounds a value larger than 1 has been established. Hill *et al.* [31] have pointed out a systematic variation of the branching ratio across the rare-earth series. Rare-earth ions with more than half-filled $4f$ shells favour enhancements at the $\mathrm{L_{III}}$ edge, those with less than half filling of the $4f$ shell tend to have larger $\mathrm{L_{II}}$ enhancements. A table of some observed branching ratios is given by Watson *et al.* [27]. For the $\mathrm{Gd^{3+}}$ ion with 7 unpaired $4f$ electrons, a branching ratio of 1 is expected and has been predicted in model calculations [32]. The branching ratio of 2.5 found in the Gd chalcogenides deviates clearly from the simple atomic picture, in which it is assumed that the $5d$ band is empty in the ground state. In the model of [32], the spectrum is determined mainly by the interactions of the excited electron with the open $4f$ and $2p$ shells. The $5d$ occupancy is neglected with the argument that the corresponding magnetic moment of 0.3 μ_B is one order of magnitude smaller than that of the $4f$ shell. The deviation from the pure d^0 L_{II}/L_{III} ratio given in [32] is a strong indication of the polarisation of the $5d$ electrons present in the ground state. Note that the effect of "breathing" *i.e.* a contraction and expansion of the $5d$ orbitals due to the $5d$-$4f$ interaction discussed in [32], can lead to an asymmetry in the line shape in addition to the interference effects discussed here. Given the limited statistical accuracy of our data, we have not made any attempt to take such an effect into account.

After discussing our findings in terms of the methodology for resonance exchange scattering, we now turn to the implications for the magnetism of GdS. We were able to show that the magnetic order of the Gd ions corresponds to type-II antiferromagnetic order on the fcc lattice, which supports earlier neutron scattering results [5]. We could not detect any magnetic signal at positions in reciprocal space not corresponding to the AF type-II order. We were able to measure the integrated intensities of six magnetic reflections and to correct for the absorption factors. A determination of the spin direction in such a highly symmetric compound based on XRES alone remains difficult due to the few available data, but also due to experimental problems, such as the uncertainties in the absorption correction and the geometrical factors arising from the finite beam and crystal sizes. Moreover, in such highly symmetric compounds the lowering of the symmetry at the magnetic phase transition gives rise to many domains. The domain population plays an important role for the measured intensities and is not known a priori. Since lattice distortions can be observed, which are connected to an elongation or compression of the [111] axis, it is reasonable to assume that domains corresponding to different symmetry-equivalent propagation directions are unequally occupied due to internal strain. From the lattice distortions alone, no deviation from the rhombohedral symmetry can be detected. This leads us to believe that domains with different symmetry-equivalent spin directions within a given set of **q**-domains are equally populated. Within this approximation, the calculated XRES intensities are extremely sensitive to the spin direction (compare Tab. 1). To give an example, the intensity of the $\frac{9}{2}\frac{1}{2}\frac{1}{2}$ reflection in our experimental units amounts to 53 for a spin direction along [111], while it amounts to 1639 for a spin direction along $[2\bar{1}\bar{1}]$. Clearly, looking at Table 1 we can exclude a spin direction along the magnetic propagation vector. However, with our limited data we can not finally decide whether the spin direction is in the [111] plane or along a [100] direction. This decision is left to our neutron data, which are very reliable, since a homogeneous beam can be assumed over the entire sample volume and since many more reflections could be measured (49 unique reflections compared to 6 for XRES). The refinement of the neutron data under the above assumptions is consistent with the interpretation that in GdS, the spin direction is perpendicular to the magnetic propagation vector. The refined value for the moment of 6.51(3) μ_B is consistent with spin 7/2, if we allow for quantum mechanical zero point spin fluctuations.

Turning now to the temperature dependence of the sublattice magnetization, we found independently with XRES and neutron diffraction a simple mean-field behaviour for $S = 7/2$ which often holds for ionic compounds. However, in the previous report on GdSe [10], a clear deviation from such a behaviour has been found with a dip in the measured intensity at approximately 37 K. It is surprising that two such similar compounds should exhibit a drastically different temperature dependence of the sublattice magnetization. One possible explanation is the strong composition dependence observed for the rare-earth chalcogenides [4]. Certainly, in our case, the $\frac{9}{2}\frac{1}{2}\frac{1}{2}$ reflection shows a smooth intensity variation following mean-field theory. This smooth intensity variation is a strong indication that the model of Hulliger and Siegrist [4] does not hold for our sample. In fact, we observe lattice anomalies at 49 and 32 K, *i.e.* at temperatures which are consistently higher than the values reported in [4]. There, the lattice distortions were reported to occur at 35 to 40 and 16 to 18 K. Hulliger and Siegrist predicted that at the first phase transition, the magnetic moments should flip from the [111] into the [110] direction. At the second phase transition, there should be a spin flip into the (111) planes. With our experiment, we are very sensitive to changes in the moment direction especially at the $\frac{9}{2}\frac{1}{2}\frac{1}{2}$ reflex. If the model of Hulliger and Siegrist was correct, we should observe at the first phase transition a large increase in intensity by a factor of roughly 18 and at the second phase transition again an increase close to a doubling of the intensity (compare Tab. 1). This is not at all consistent with our observation, in which the $\frac{9}{2}\frac{1}{2}\frac{1}{2}$ intensity variation with temperature is very smooth and shows no anomalies at the temperatures where the Bragg peaks split. One could argue that with XRES, we are only sensitive to a near-surface layer of some 3 μm thickness. In this layer, the moment orientation could deviate from the bulk. However, our neutron results depicted in Figure 4 also show no indications for a spin reorientation. Therefore, we do not believe that spin flips occur below the Néel temperature. The spin direction remains the same throughout the ordered phase. In this case, the question arises, what drives the low-temperature phase transitions, if not the anisotropic exchange suggested by Hulliger and Siegrist. Anisotropic exchange interactions can only be very weak in these compounds with an orbital $L = 0$ ground state. On the other hand, magnetization measurements [6] indicate the existence of higher-order exchange interactions, such as biquadratic exchange (proportional to $(\mathbf{S}_i \cdot \mathbf{S}_j)^2$) or three spin interactions (proportional to $(\mathbf{S}_i \cdot \mathbf{S}_k)(\mathbf{S}_k \cdot \mathbf{S}_j)$). These interactions can give rise to additional low temperature phase transitions, as can be easily shown for the case of a simple two-sublattice antiferromagnet with bilinear and biquadratic exchange only. With the sublattice magnetizations $\mathbf{M}_A$ and $\mathbf{M}_B$ for the two sublattices, the relevant parts of the free-energy density can be written as

$$F/V = \beta(\mathbf{M}_A \cdot \mathbf{M}_B)^2 - \alpha\,\mathbf{M}_A \cdot \mathbf{M}_B. \qquad (11)$$

The angle φ between the sublattice magnetization $\mathbf{M}_\mathrm{A}$ and $\mathbf{M}_\mathrm{B}$ can be obtained from the condition $\left(\frac{\delta F}{\delta\varphi}\right)_T = 0$ and for antiferromagnetic bilinear exchange ($\alpha < 0$), we obtain the following solutions:

$$\begin{aligned} &\alpha < 0, \beta < 0: \quad \varphi = \pi \\ &\alpha < 0, \beta > 0: \quad \varphi = \pi \quad \text{for} \quad M^2 < \frac{-\alpha}{2\beta} \\ &\qquad\qquad\qquad \cos\varphi = \frac{\alpha}{2\beta M^2} \quad \text{for} \quad M^2 > \frac{-\alpha}{2\beta}\,. \end{aligned} \tag{12}$$

For $\beta < 0$ no additional phase transitions occur. For $\beta > 0$ a collinear antiferromagnetic structure is realized close to T_N. At lower temperatures, as M^2 exceeds $\frac{-\alpha}{2\beta}$, a canted antiferromagnetic structure is predicted with a smooth temperature variation of the canting angle φ. In a multidomain sample, it is very difficult to observe such a canting with diffraction methods. However, for the canting to occur, the energy density for biquadratic exchange has to be comparable to the energy density for bilinear exchange. On the other hand it has been shown in [33] that even a small contribution of biquadratic exchange drastically alters the shape of the sublattice magnetization curves, a prediction which is inconsistent with our observation of a simple mean-field curve. Therefore, within the present study, the driving forces for the low-temperature phase transitions could not be identified.

That GdS is indeed a very isotropic magnetic system is proven by the critical behaviour close to the Néel temperature. Since in such a highly symmetric compound, the critical fluctuations occur around all symmetry-equivalent positions in reciprocal space, the diffuse scattering for a given magnetic superlattice point is rather weak. Therefore, we could only measure the critical behaviour of the sublattice magnetization and not those of the susceptibility and the correlation length. In two independent experiments with different momentum space resolutions, a critical exponent β was determined, which agrees very well with the predictions of renormalisation group theory for a pure Heisenberg model [34]. While the weakness of the signal above T_N did not allow a detailed analysis of the critical diffuse scattering, it still became clear that a sharp component persists up to several degrees above T_N. This sharp component has been observed in many other magnetic and non-magnetic systems (*e.g.* [35–37]). It is believed that this component is connected with scattering from a near-surface layer and should therefore be enhanced for our experiments at the absorption edges.

6 Summary and conclusions

In summary we were able to show how X-ray resonance exchange scattering can be an important complementary tool to neutron scattering for the study of the magnetism of strongly neutron-absorbing materials. By polarisation analysis, we could show that in GdS, dipolar transitions largely dominate the resonances at the $\mathrm{L_{II}}$ and $\mathrm{L_{III}}$ absorption edges. By comparing to neutron diffraction, we could prove that the resonance signal is indeed proportional to the square of the order parameter. We observed a temperature dependence characteristic for a $S = 7/2$ system, which gives evidence of the intimate coupling of the $5d$ and $4f$ systems. The asymmetry of the resonance line shapes could be interpreted as an interference effect between non-resonant magnetic scattering and resonance exchange scattering. The branching ratio of 2.5 between the $\mathrm{L_{II}}$ and $\mathrm{L_{III}}$ absorption edges deviates from the pure d^0 value of 1 giving a strong indication for the polarisation of the $5d$ electrons.

We could verify that GdS shows antiferromagnetic type II order. Under the assumption of an equal population of S-domains, a refinement of the neutron diffraction data gave a spin direction perpendicular to the magnetic propagation vector with a value for the sublattice magnetisation of 6.51(3) μ_B. While we could observe lattice distortions below the Néel temperature, we did not find any indications that these distortions are connected with spin-flip transitions. In agreement with the pure $L = 0$ ground state, we found the critical behaviour for the sublattice magnetisation to be Heisenberg-like. A sharp component in the critical scattering was observed above the Néel temperature.

The XRES study of GdS presented here forms the basis for a study of the mixed crystal system $\mathrm{Gd}_x\mathrm{Eu}_{1-x}\mathrm{S}$, which will be presented in a following paper [38]. In this study, XRES has been used to determine element-specific magnetic order in this spin glass system.

We want to thank Mrs. Cornelisen, University of Hamburg, for performing the microprobe analysis. We have benefited from discussions with J.R. Schneider and U. Köbler. Financial support was provided by the BMBF under contract number 03-BR4DES-2.

Appendix A: Absorption correction

In Figure A.1 the geometry of the scattering process used for the absorption correction is depicted. In all of our experiments, the sample can be described as a platelet of infinite surface area (the crystal dimensions were always much larger than the beamsize) and of infinite thickness (the crystals were several mm thick compared to an absorption length of some μm). The incident beam can be described by the intensity I_0, the unit wave vector $\hat{\mathbf{k}}$, the photon energy E and the angle of incidence α. The corresponding quantities for the scattered beam are denoted by I', $\hat{\mathbf{k}}'$, E' and β. $j_0(x,y)$ denotes the incident flux distribution in the beam. Along ξ the intensity decays according to:

$$j(\xi; x, y) = j_0(x, y)\mathrm{e}^{-\mu(E)\xi}. \tag{A.1}$$

If a photon is absorbed at depth z, the probability that a fluorescence photon is being emitted into the direction of $\hat{\mathbf{k}}'$ is:

$$W = \frac{1}{4\pi}\omega\mu^X(E)\,\Delta\Omega\,\mathrm{d}\xi. \tag{A.2}$$

$$\mu^X(E) = \frac{\left\{\left[I^{\mathrm{F}}(E)\left(\mu(E_1)\,f(E) + \mu(E_{\mathrm{F}})\frac{\sin\alpha}{\sin\beta}\right) - I^{\mathrm{F}}(E_1)\,f(E)\left(\mu(E_1) + \mu(E_{\mathrm{F}})\frac{\sin\alpha}{\sin\beta}\right)\right][\mu(E_2) - \mu(E_1)f(E_2)]\right\}}{\left\{I^{\mathrm{F}}(E_2)\left(\mu(E_2) + \mu(E_{\mathrm{F}})\frac{\sin\alpha}{\sin\beta}\right) - I^{\mathrm{F}}(E_1)\left(\mu(E_1) + \mu(E_{\mathrm{F}})\frac{\sin\alpha}{\sin\beta}\right) f(E_2) - I^{\mathrm{F}}(E)(\mu(E_2) - \mu(E_1)f(E_2))\right\}} \cdot \qquad \text{(A.8)}$$

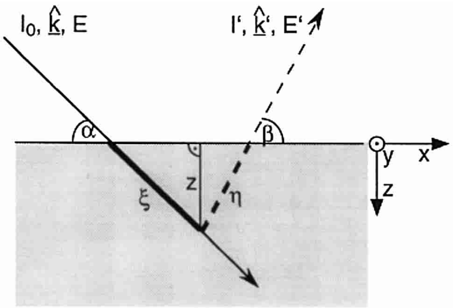

Fig. A.1. Geometry of the scattering process assumed for the absorption correction.

Here $\mu^X(E)$ is the resonant contribution to the absorption coefficient (see below), ω the fluorescence yield and $\Delta\Omega$ the solid-angle element in $\hat{\mathbf{k}}'$ direction. The intensity contribution from the depth z scattered into the detector element $\Delta\Omega$ is given by

$$\begin{aligned} \mathrm{d}j'(z;x,y) &= j(\xi;x,y)\,\mathrm{d}\xi\frac{\omega\mu^X(E)}{4\pi}\,\Delta\Omega\,\mathrm{e}^{-\mu(E')\eta} \\ &= j_0(x,y)\,\mathrm{e}^{-\left(\mu(E)\frac{z}{\sin\alpha}+\mu(E')\frac{z}{\sin\beta}\right)} \\ &\quad\times\frac{\omega\mu^X(E)}{4\pi}\,\Delta\Omega\,\mathrm{d}\left(\frac{z}{\sin\alpha}\right)\cdot \end{aligned} \qquad \text{(A.3)}$$

The total intensity is obtained by integrating (A.3) and one obtains:

$$I' = \int \mathrm{d}x\mathrm{d}y\mathrm{d}j' = I_0\omega\mu^X(E)\frac{\Delta\Omega}{4\pi}\frac{1}{\mu(E) + \mu(E')\dfrac{\sin\alpha}{\sin\beta}}\cdot \qquad \text{(A.4)}$$

In the vicinity of the edge, one fluorescence line changes drastically in intensity as can be seen in Figure 1. This intensity variation can be taken as a measure of the variation of the absorption cross section through the edge. Besides this resonant contribution $\mu^X(E)$, a slowly varying contribution $\mu^{\mathrm{R}}(E)$ has to be considered to give the absorption coefficient:

$$\mu(E) = \mu^{\mathrm{R}}(E) + \mu^X(E). \qquad \text{(A.5)}$$

In many cases, the slowly varying part μ^{R} can be described by $\mu^{\mathrm{R}} \propto \lambda^3$. In what follows, we assume that two energies E_1 and E_2 well below and well above the absorption edge exist, for which tabulated values of $\mu(E)$ can be found. These reference energies are used to determine the absolute value of the absorption coefficient, while its variation throughout the edge is obtained from the energy dependence of the fluorescence yield. In what follows, we assume the following functional form for μ^{R}:

$$\mu^{\mathrm{R}}(E) = \mu(E_1)\,f(E,E_1) \quad \text{with} \quad f(E,E_1) := f(E) := E_1^3/E^3. \qquad \text{(A.6)}$$

E_1 was chosen so that μ^X vanishes, which implies $\mu(E_1) = \mu^{\mathrm{R}}(E_1)$. The intensity in the fluorescence channel has a background contribution and the fluorescence contribution at the X edge.

These intensities have to be absorption corrected according to (A.4) to yield the following expression for the total fluorescence intensity:

$$I^F(E) = \frac{C_1\,f(E) + C_2\mu^X(E)}{\mu(E_1)f(E) + \mu^X(E) + \mu(E_{\mathrm{F}})\dfrac{\sin\alpha}{\sin\beta}}\cdot \qquad \text{(A.7)}$$

The photon energies E_1, E_2 and the energy of the fluorescence photon E_{F} are far from the energy of the absorption edge and thus can safely be taken from tabulated values [39]. The measured values of the fluorescence intensities at the energies E_1 and E_2 can then be used to determine the coefficients C_1 and C_2. With these values of the coefficients C_1 and C_2, μ^X can be obtained from the measured fluorescence intensities as follows:

see equation (A.8) above

Finally the total absorption coefficient $\mu(E)$ is given by the sum of the background and edge contribution according to (A.5) and (A.6). With this coefficient $\mu(E)$, the Bragg data can be corrected using

$$I' = I_0\frac{1}{\mu(E)\left(1 + \dfrac{\sin\alpha}{\sin\beta}\right)}\cdot \qquad \text{(A.9)}$$

References

1. O. Vogt, K. Mattenberger, *Magnetic Measurements on Rare-Earth and Actinide Monopnictides and Monochalcogenides*, Chap. 114, in *Handbook on the Physics and Chemistry of Rare-Earth*, Vol. 17, edited by K.A. Gschneidner, L. Eyring, G.H. Lander, G.R. Choppin (Elsevier Science Publishers, 1993).
2. D.E. Eastman, M. Kuznietz, Phys. Rev. Lett. **26**, 846 (1971).
3. P. Wachter, Physics Reports **44**, 159 (1978).
4. F. Hulliger, T. Siegrist, Z. Physik B **35**, 81 (1979).
5. T.R. McGuire, R.J. Gambino, S.J. Pickart, H.A. Alperin, J. Appl. Phys. **40**, 1009 (1969).

6. U. Köbler, D. Hupfeld, W. Schnelle, K. Mattenberger, Th. Brückel, JMMM **205**, 90 (1999).
7. D. Gibbs, D.R. Harshman, E.D. Isaacs, D.B. McWhan, D. Mills, C. Vettier, Phys. Rev. Lett. **61**, 1241 (1988).
8. J.P. Hannon, G.T. Trammell, M. Blume, D. Gibbs, Phys. Rev. Lett. **61**, 1245 (1988). Phys. Rev. Lett. **62**, 2644 (E) (1989).
9. J. Luo, G.T. Trammell, J.P. Hannon, Phys. Rev. Lett. **71**, 287 (1993).
10. M.M.R. Costa, M.J.M. de Almeida, W.J. Nuttall, W.G. Stirling, C.C. Tang, J.B. Forsyth, M.J. Cooper, J. Phys. Cond. Matt. **8**, 2425 (1996).
11. M. Blume, J. Appl. Phys. **57**, 3615 (1985).
12. M. Blume, D. Gibbs, Phys. Rev. B **37**, 1779 (1988).
13. M. Blume, in *Resonant Anomalous X-Ray Scattering*, edited by G. Materlik, C.J. Sparks, K. Fischer (Elsevier Science, 1994).
14. E.D. Isaacs, D.B. McWhan, C. Peters, G.E. Ice, D.P. Siddons, J.B. Hastings, C. Vettier, O. Vogt, Phys. Rev. Lett. **62**, 1671 (1989).
15. Th. Brückel, Acta Phys. Pol. A **91**, 669 (1997).
16. J.P. Hill, D.F. McMorrow, Acta Cryst. A **52**, 236 (1996).
17. K. Mattenberger, L. Scherrer, O. Vogt, J. Cryst. Growth **67**, 467 (1984).
18. Th. Brückel, D. Hupfeld, J. Strempfer (to be published).
19. Th. Brückel, R. Nowak, Th. Köhler, U. Brüggmann, U. Maul, E. Pfützenreuter, V. Rilling, W. Prandl, J. Appl. Cryst. **29**, 686 (1996).
20. Th. Brückel, M. Lippert, Th. Köhler, J. R. Schneider, W. Prandl, V. Rilling, M. Schilling, Acta Cryst. A **52**, 427 (1996).
21. S.C. Perry, M.M.R. Costa, W.G. Stirling, M.J. Longfield, D. Mannix, Th. Brückel, J. Phys. Cond. Matt. **10**, 1951 (1998).
22. J. Bohr, D. Gibbs, K. Huang, Phys. Rev. B **42**, 4322 (1990).
23. E.D. Isaacs, D.B. McWhan, D.P. Siddons, J.B. Hastings, D. Gibbs, Phys. Rev. B **40**, 9336 (1989).
24. D. Gibbs, J. Bohr, J.D. Axe, D.E. Moncton, K.L. D'Amico, Phys. Rev. B **34**, 8182 (1986).
25. G. Helgesen, J.P. Hill, T.R. Thurston, D. Gibbs, Phys. Rev. B **52** , 9446 (1995).
26. D. Gibbs, G. Grübel, D.R. Harshman, D.E. Isaacs, D.B. McWhan, D. Mills, C. Vettier, Phys. Rev. B **43**, 5663 (1991).
27. D. Watson, E.M. Forgan, W.J. Nuttall, W.G. Stirling, D. Fort, Phys. Rev. B. **53**, 726 (1996).
28. M.K. Sanyal, D. Gibbs, J. Bohr, M. Wulff, Phys. Rev. B **49**, 1079 (1994).
29. M.O. Krause, J.H. Oliver, J. Phys. Chem. Ref. Data **8**, 329 (1979).
30. U. Arp, G. Materlik, M. Richter, B. Sonntag, J. Phys. B **23**, L811 (1990).
31. J.P. Hill, A. Vigliante, D. Gibbs, J.L. Peng, R.L. Greene, Phys. Rev. B **52**, 6575 (1995).
32. M. van Veenendaal, J.B. Goedkoop, B.T. Thole, Phys. Rev. Lett. **78**, 1162 (1997).
33. D.S. Rodbell, I.S. Jacobs, J. Owen, E.A. Harris, Phys. Rev. Lett. **11**, 10 (1963).
34. M.F. Collins, *Magnetic Critical Scattering* (Oxford University Press, 1989).
35. T.R. Thurston, G. Helgesen, D. Gibbs, J.P. Hill, B.D. Gaulin, G. Shirane, Phys. Rev. Lett. **70**, 3151 (1993).
36. S.C. Perry, W.J. Nuttall, W.G. Stirling, G.H. Lander, O. Vogt, Phys. Rev. B **54**, 15234 (1996).
37. U. Rütt, A. Diederichs, J.R. Schneider, G. Shirane, Europhys. Lett. **39**, 395 (1997).
38. D. Hupfeld, W. Schweika, J. Strempfer, K. Mattenberger, G.J. McIntyre, Th. Brückel, Europhys. Lett. **49**, 92 (2000).
39. S. Brennan, P.L. Cowan, Rev. Sci. Inst. **63**, 850 (1992).